Supporting Information

Scalable 3-D Carbon Nitride Sponge as an Efficient Metal-Free Bifunctional Oxygen Electrocatalyst for Rechargeable Zn-Air Batteries

Sambhaji S. Shinde[†], Chi-Ho Lee[‡], Abdul Sami[†], Dong-Hyung Kim[†], Sang-Uck Lee[‡#*], Jung-Ho Lee[†*]

[†]*Department of Materials and Chemical Engineering, Hanyang University, Ansan, Kyunggido, 426-791, Republic of Korea*

[‡]*Department of Bionano Technology, Hanyang University, Ansan, Kyunggido, 426-791, Republic of Korea*

[#]*Department of Applied Chemistry, Hanyang University, Ansan, Kyunggido, 426-791, Republic of Korea*

E-mail: jungho@hanyang.ac.kr, sulee@hanyang.ac.kr.

Experimental Methods

Materials characterization

The microstructure and morphology were investigated using a field-emission scanning electron microscope (FESEM; JEOL-6700F) and a transmission electron microscope (TEM; JEOL, JEM-2010). The energy dispersive X-ray spectroscopy (EDS) elemental mapping images were recorded on a JEOL-6700 microscope. X-ray photoelectron spectra (XPS) were measured using a VG SCIENTA (R 3000) spectrometer equipped with an Al Kα source (1486.6 eV). The specific surface areas (Brunauer–Emmett–Teller (BET) method) and pore size distribution (Barrett, Joyner, and Halenda (BJH) method) were examined using nitrogen adsorption−desorption isotherms measured on an AUTOSORB-1-MP system at 77 K. XRD patterns were collected using a Rigaku D/MAX-2500 X-ray diffractometer (Cu Kα, λ = 1.5406 Å). Fourier transform infrared spectra (FITR) were recorded on a PerkinElmer spectrum GX FTIR unit. Electrochemical tests were performed using a CHI 760 D electrochemical workstation (CH Instruments, Inc., USA).

Electrochemical measurements

The electrochemical activities of the catalysts were measured using a standard three-electrode electrochemical cell filled with a 0.1 M KOH electrolyte. To prepare the working electrode, the catalysts (5.0 mg) and 60 µl of a 5 wt% Nafion solution were dispersed in 1 ml of ethanol. The resulting mixture was sonicated to form a homogeneous ink. A catalyst loading of 0.15 mg cm^{-2} was applied on the polished surface of the glassy carbon electrode by the dropwise addition of 5 µl of catalyst ink, and the sample was dried at room temperature. A Pt wire and Ag/AgCl electrode were used as the counter and reference electrodes, respectively. The electrochemical impedance spectroscopy measurements were carried out in a frequency range

of 1 MHz–0.01 Hz with amplitude of 5 mV. The current density was normalized to the geometrical surface area, and the measured potentials *vs.* Ag/AgCl were converted to a reversible hydrogen electrode (RHE) scale according to the Nernst equation ($E_{RHE} = E_{Ag/Ag/Cl}$ + 0.205+ 0.059 × pH). A flow of O_2 was maintained over the electrolyte during the measurement to ensure its continued O_2 saturation. Polarization data were measured using linear sweep voltammetry at a scan rate of 5 mV s^{-1} with automatic iR compensation.

The Koutecky-Levich equation was used to determine the electron transfer number (n) for the ORR process:

$$\frac{1}{J} = \frac{1}{J_K} + \frac{1}{B\omega^{1/2}}$$

$$B = 0.2nFC_O(D_O)^{2/3}\nu^{-1/6}$$

where J is the measured current, J_K is the kinetic current, ω is the electrode rotation rate in rpm, F is the Faraday constant (96485 C mol^{-1}), C_O is the bulk concentration of O_2(1.2×10^{-6} mol cm^{-3}), D_O is the diffusion coefficient of O_2 (1.9×10^{-5} cm^2 s^{-1}), and ν is the kinematic viscosity of electrolyte (0.01 cm^2 s^{-1}). The constant 0.2 is adopted when the rotation speed is expressed in rpm. The peroxide yields (H_2O^-) and number of transferred electrons (n) were calculated using the equations below:

$$H_2O^-(\%) = 100\frac{2I_r/N}{I_d + I_r/N}$$

$$n = 4\frac{I_d}{I_d + I_r/N}$$

where I_d is the disk current, I_r is the ring current, and N the is current collection efficiency of the Pt ring. N was determined to be 0.41.

Zn-air battery performance

For the Zn–air battery test, 6 M KOH was used as the electrolyte, with a polished zinc plate as the anode. The air cathode was prepared by uniformly coating the prepared catalyst ink onto carbon fiber paper (SPECTRACARB 2040-A, Fuel Cell store) followed by drying at 60 °C. Both electrodes were assembled into a home-made Zn–air battery. A similar process was adopted to prepare air electrodes with a catalyst mass ratio of 1:3 as the ORR and OER electrodes in order to investigate the performance of a three-electrode rechargeable Zn–air battery.

RESULTS AND DISCUSSION

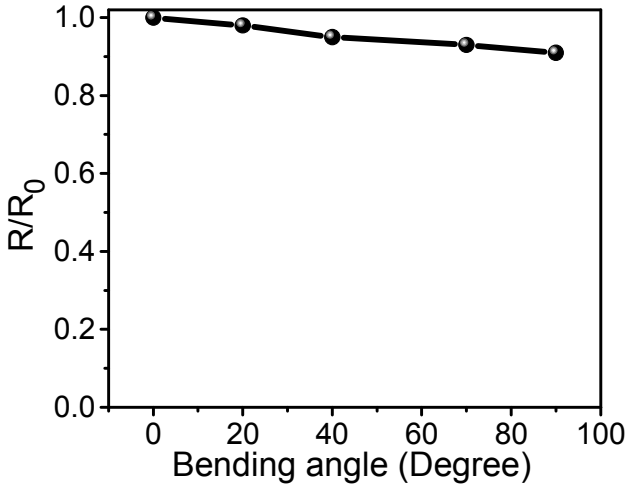

Figure S1. Resistance changes of P,S-CNS with the increase of bending angle.

The flexible structure was further confirmed by measuring the electrical conductivity under bending test. A slight decrement in resistances of P,S-CNS with increasing bending angles confirms the interconnecting feature of P,S-CNS with the increase of bending angle.[S1]

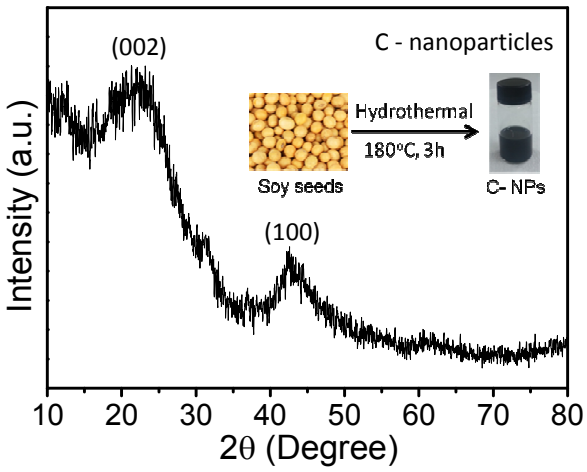

Figure S2. X-ray diffraction pattern of prepared carbon nanoparticles. The inset shows the corresponding synthesis process.

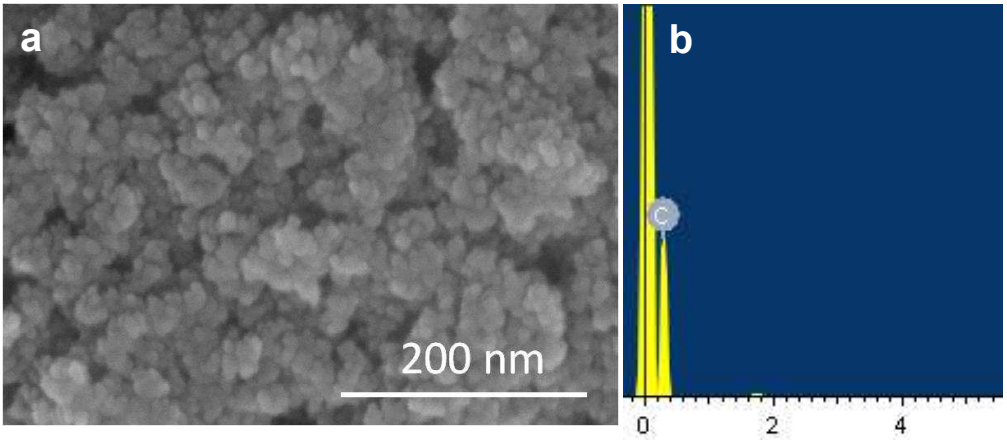

Figure S3. (a) Scanning electron microscopy image of prepared carbon nanoparticles and (b) corresponding EDS spectrum.

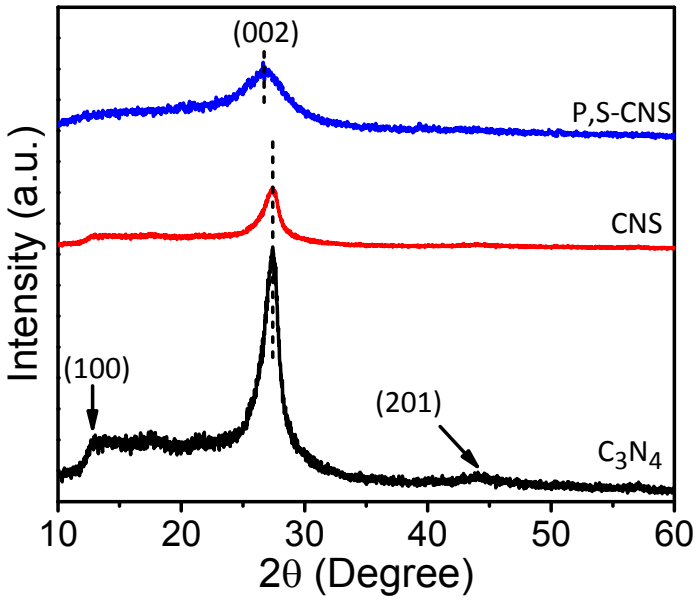

Figure S4. X-ray diffraction patterns of pristine C_3N_4, CNS, and P,S-CNS catalysts.

The phase structure of prepared catalysts was determined using XRD. Two pronounced peaks at 13.01, and 27.43^o in bulk C_3N_4, CNS, and P,S-CNS catalysts, corresponded to the in-plane packing motif and interlayer stacking of aromatic segments, which were assigned as (100) and (002) peaks, respectively.[S2] The low-angle peak at 13.01^o became weaker in the CNS and P,S-CNS. However, the characteristic interlayer stacking peak (002) of aromatic systems was red shifted (26.71^o) and was considerably broader than that of bulk C_3N_4 and CNS. These results clearly indicate the successful formation P, S co-doped carbon nitride decorated with CNPs.

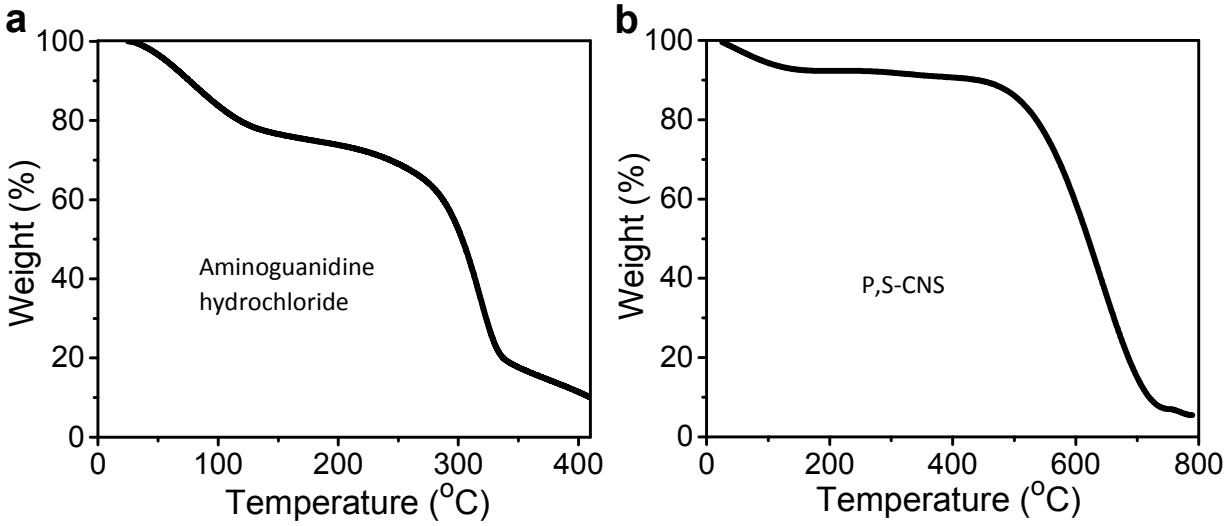

Figure S5. (a) Thermogravimetric (TG) curve of aminoguanidine hydrochloride, which indicates that the majority of the organic motif decomposes in the range of 100-340 ^{o}C. (b) Thermogravimetric (TG) curve of P,S-CNS hybrid catalyst. The P,S-CNS was found to be stable up to ~500 ^{o}C, implying stable construction from tetrazine-base units in the materials. But, it decomposes slowly upon increasing temperature above 500 ^{o}C revealing a high thermal stability.

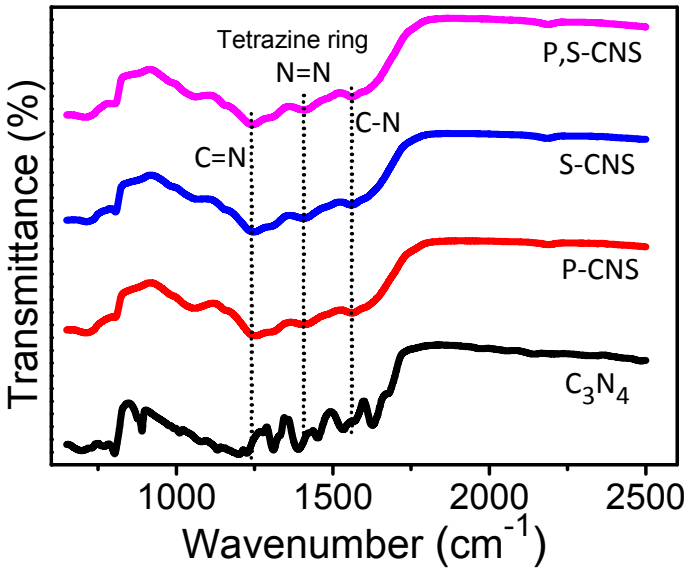

Figure S6. FTIR spectra of C_3N_4, P-CNS, S-CNS, and P, S-CNS catalysts.

The prepared C_3N_4, P-CNS, S-CNS, and P, S-CNS were characterized by FT-IR spectra to confirm their molecular structures. A characteristic breathing mode of the s-triazine ring system at 806-879 cm^{-1} was observed for C_3N_4.[S3] In the 1100-1650 cm^{-1} region, the peaks at 1228, 1309, 1390, 1452, 1533, 1567, and 1629 cm^{-1} corresponded to the typical stretching vibration modes of C=N and C-N heterocycles.[S4] For P-CNS, S-CNS, and P,S-CNS catalysts, the peaks observed in the region of 720-800 cm^{-1} were characteristics of synphase and antiphase vibrations of N=N of the tetrazine ring. The peaks at 1312 and 1409 cm^{-1} were attributed to C=N and N=N stretching bonds, respectively, and these results are consistent with N 1s XPS spectra. A peak associated with a graphitic C-N band was observed at 1560 cm^{-1}, and this was mainly attributed to the aromatic ring modes. One new band around 1050 cm^{-1} was attributed to the P-N stretching mode.[S5] The small band observed at 2187 cm^{-1} was attributed to N=C=O stretching due to pyridinic N^+O^- and was confirmed by XPS measurements. Also, the P-CNS, S-CNS, and P, S-CNS (1640 cm^{-1}) showed apparent shifts in the stretching modes of CN heterocycles compared to bulk C_3N_4 (1629 cm^{-1}). These spectroscopic results confirmed the formation of polymeric CN structures in the samples.

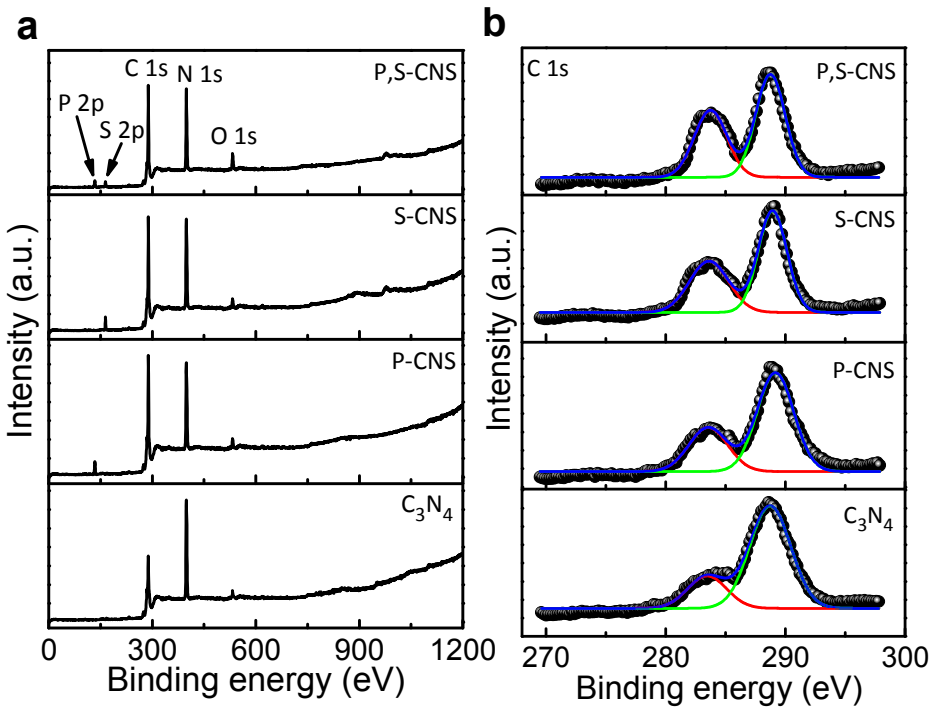

Figure S7. (a) XPS survey scan spectra and (b) curve-fitted high-resolution XPS spectra of C 1s for C_3N_4, P-CNS, S-CNS, and P,S-CNS. The absence of any metal-related signals confirmed that the prepared CNSs were strictly metal-free.

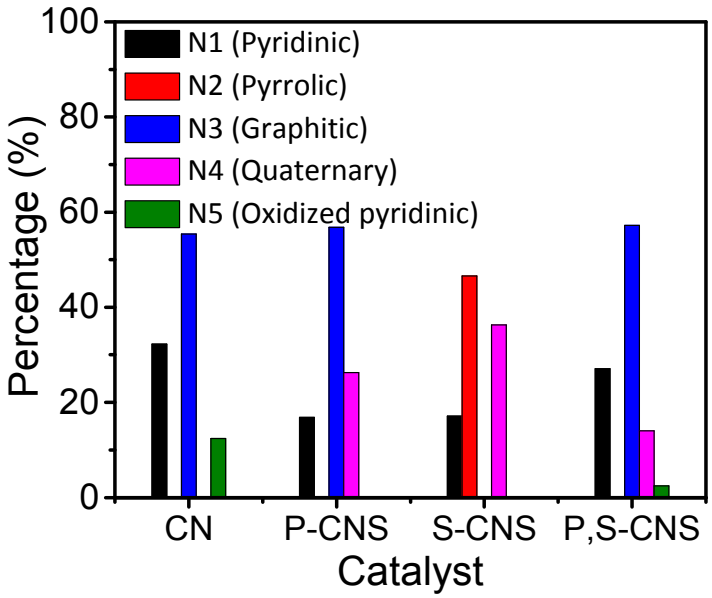

Figure S8. Quantification of the types of nitrogen in terms of relative percentages of total nitrogen content in C_3N_4, P-CNS, S-CNS, and P, S-CNS catalysts.

Figure S9. Digital image of the electrocatalytic measurement in a three-electrode glass cell with P,S-CNS grown on carbon fiber paper directly used as the working electrode.

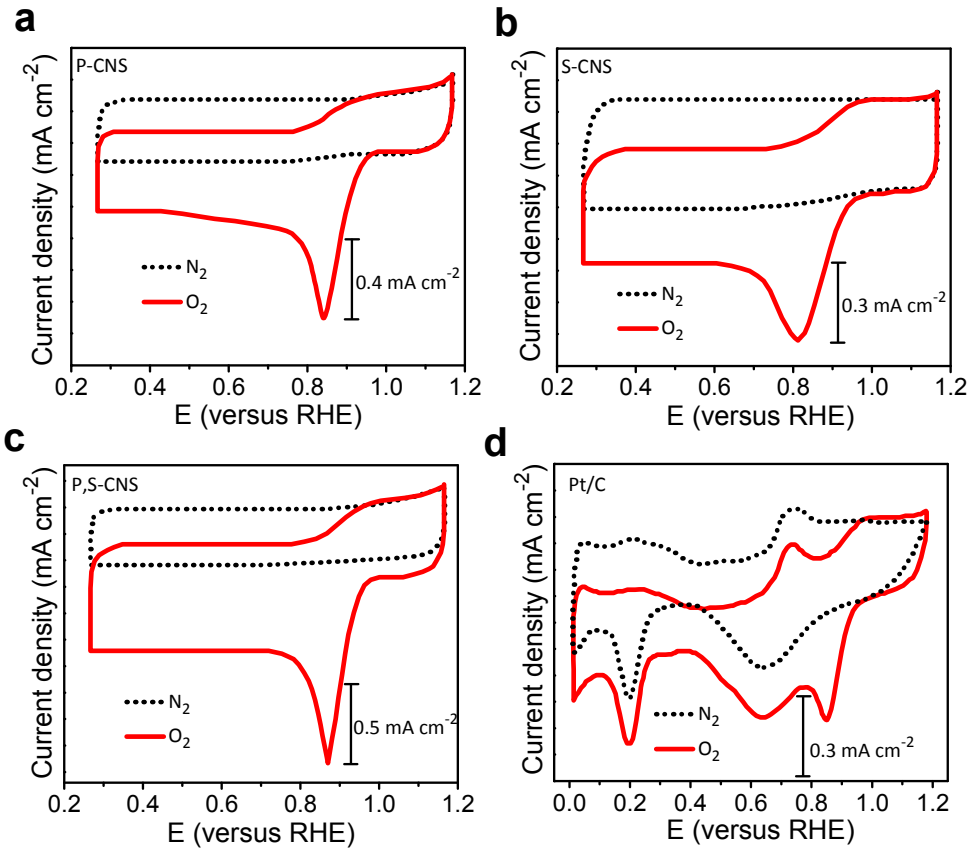

Figure S10. (a) Cyclic voltammetry curves of (a) P-CNS, (b) S-CNS, (c) P,S-CNS, and (d) commercial Pt/C catalysts in N_2- and O_2-saturated 0.1 M aqueous KOH electrolyte solutions.

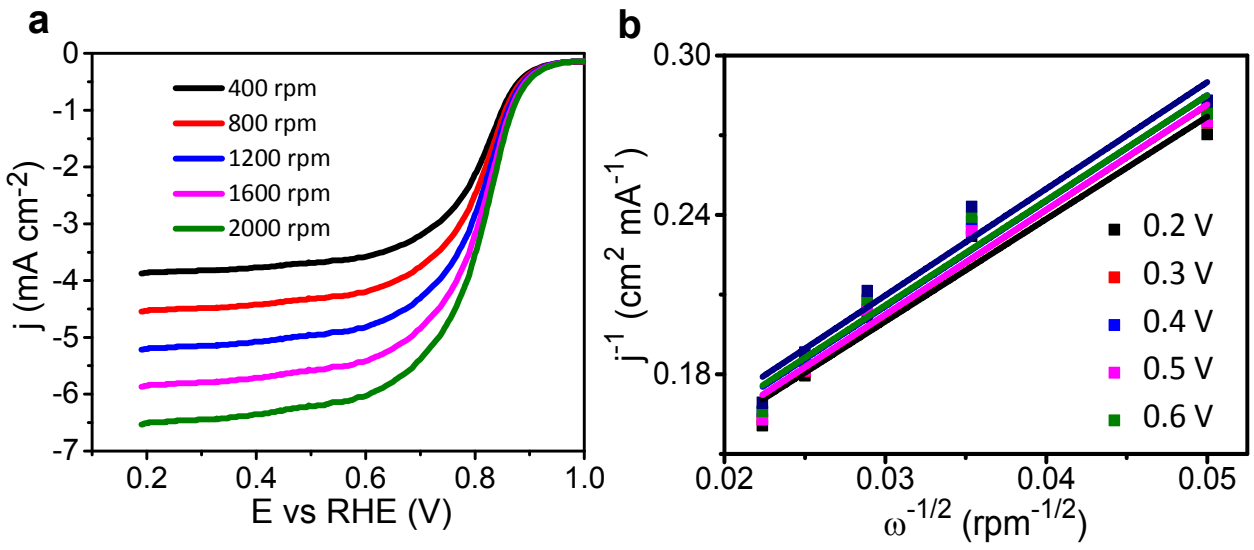

Figure S11. (a) RDE polarization curves of Pt/C for ORR at different rotating speeds, and (b) corresponding K-L plots at different potentials.

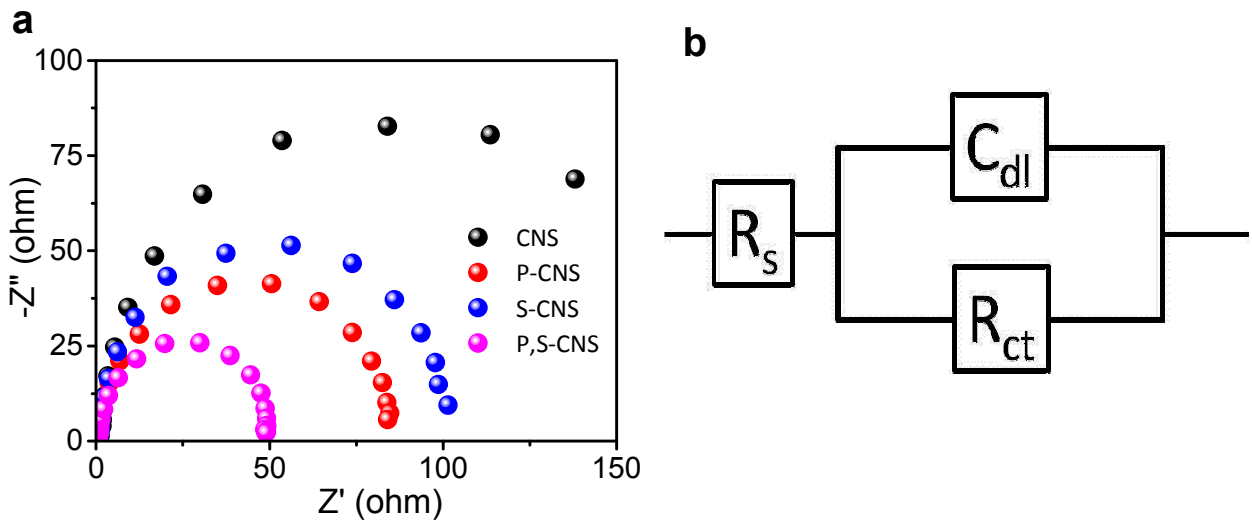

Figure S12. Electrochemical impedance spectra (EIS) of CNS, P-CNS, S-CNS, and P,S-CNS catalysts at -0.2 V *vs* RHE in 0.1 M KOH, and (b) the corresponding equivalent circuit. The semicircular diameter of EIS measured for P,S-CNS is much smaller than that of CNS, indicating smaller contact and charge transfer impedance caused by the synergistic effects of P and S doping, which are beneficial for electrocatalytic applications.

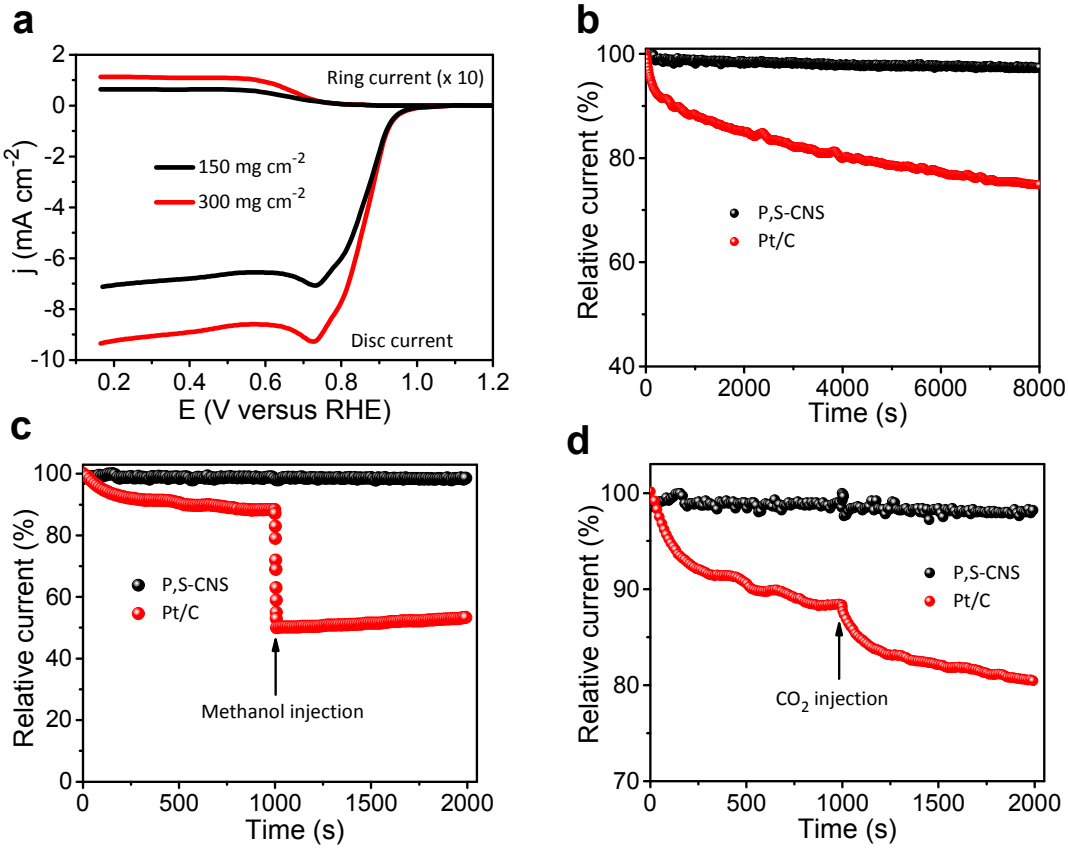

Figure S13. (a) RRDE measurements (1600 rpm) for ORR the at a P,S-CNS electrode with different catalyst loadings. (b) ORR chronoamperometric response of P,S-CNS and Pt/C in O_2 saturated 0.1 M KOH. (c) Chronoamperometric responses in O_2-saturated 0.1 M KOH at P,S-CNS and Pt/C catalysts before and after addition of 2 M methanol. (d) CO poisoning tests.

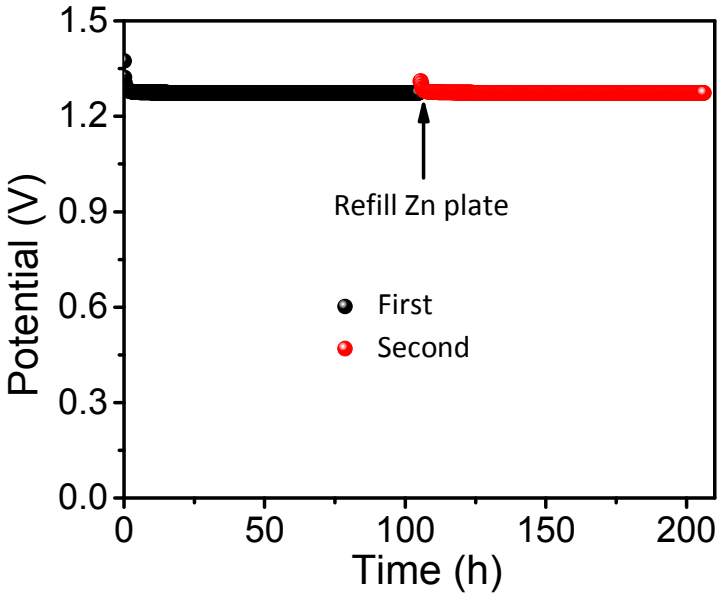

Figure S14. Mechanical recharge cycles for the primary Zn-air battery with P,S-CNS catalysts at 2 mA cm^{-2}.

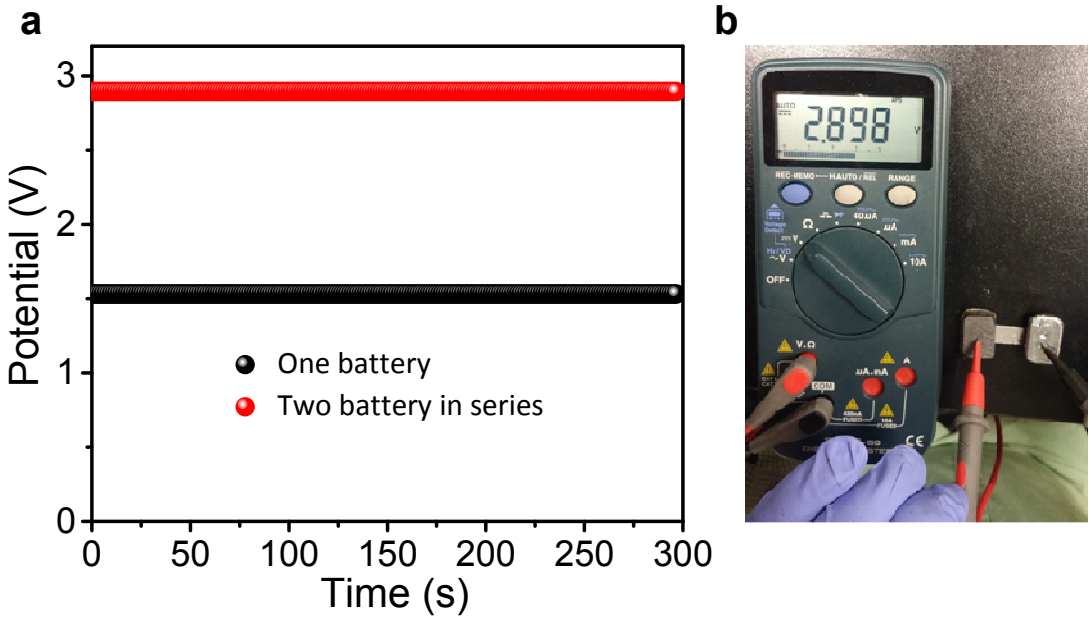

Figure S15. (a) Open circuit potentials of Zn-air battery and two batteries in series. (b) Photograph of two Zn-air batteries in series with an open circuit voltage of 2.898 V.

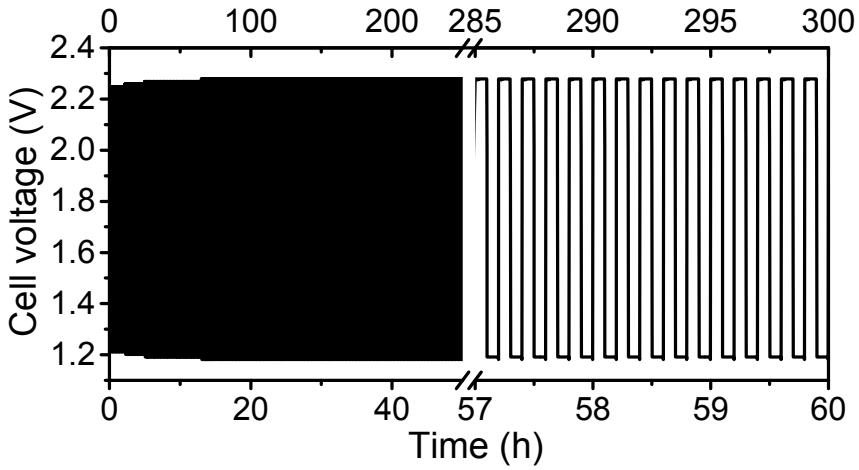

Figure S16. Charge/discharge cycling curves of a tri-electrode Zn-air battery using Pt/C and RuO_2 as catalysts in 6 M KOH electrolyte for the ORR and OER, respectively.

Supplementary tables

Table S1 Elemental compositions of the prepared P-CNS, S-CNS, and P,S-CNS samples.

Sample	C (%)	N (%)	P (%)	S (%)
C_3N_4	42.04	56.60	-	-
P-CNS	53.32	41.71	3.36	-
S-CNS	54.15	41.26	-	3.11
P,S-CNS	53.55	41.36	1.68	1.59

Table S2. The various nitrogen moieties as designated for the C_3N_4, P-CNS, S-CNS, and P, S-CNS catalysts: N1 (pyridinic), N2 (pyrrolic), N3 (graphitic), N4 (quaternary) and N5 (pyridinic N^+O^-). Note that quaternary N can induce a non-uniform electron density distribution on adjacent carbon atoms and facilitate O_2 adsorption and dissociation, thus functioning as an efficient active site for the ORR.

Sample	N1 (%)	N2 (%)	N3 (%)	N4 (%)	N5 (%)
C_3N_4	398.81	-	400.38	-	402.53
P-CNS	398.10	-	400.02	401.66	-
S-CNS	398.09	399.67	-	401.16	-
P,S-CNS	398.83	-	400.16	401.89	403.72

Table S3. A comparison of the electrocatalytic activity of recently reported highly active ORR/OER bifunctional oxygen catalysts.

Catalyst	Loading (mg cm^{-2})	ORR onset potential (V *vs*. RHE)	ORR Tafel slope (mV dec^{-1})	ORR half-wave potential ($E_{1/2}$) (V *vs*. RHE)	OER onset potential (V *vs*. RHE)	OER Tafel slope (mV dec^{-1})	OER potential @ 10 mA cm^{-2} ($E_{j=10}$) (V *vs*. RHE)	Overall oxygen electrode activity ΔE ($E_{j=10} - E_{1/2}$) (V)	Reference
PS-CNS	0.15	0.97	61	0.87	1.26	64	1.56	0.69	This work
PCN-CFP	0.20	0.94	122.3	0.67	1.53	61.6	1.63	0.96	S6
NPMC-1000	0.15	0.94	-	0.85	1.30	-	-	-	S7
N-G/CNT	0.25	0.88	-	0.63	1.50	83	1.63	1.00	S8
Mn_xO_y/N-C	0.21	0.85	-	0.81	1.55	82.6	1.68	0.87	S9
Co_3O_4/CO_2MnO_4	0.1	0.90	-	0.68	1.57	-	1.77	1.09	S10
CoO/N-G	0.7	0.90	48	0.81	1.30	71	1.57	0.76	S11
NCNF-1000	0.1	0.94		0.85	1.30		1.84	1.02	S12
Cu-MOF/GO	0.23	0.29	69	-	1.19	65	1.59	-	S13
Fe@NC	0.31	0.96	-	0.83	1.52	-	1.71	0.88	S14

Table S4. The performance of primary Zn-air batteries with various electrocatalysts.

Catalyst	OCP (V)	Power density (mW cm^{-2})	Specific capacity (mA h g^{-1})	Durability (h)	Reference
PS-CNS	1.51	198	830	210 (~1.3 V)	This work
FePc-Py-CNTs	-	-	-	100 (~1.2 V)	S15
CoO/N-CNT	1.4	265	570	-	S16
N, B-CNT	-	25	-	30 (~1.1 V)	S17
NiC_2O_4	-	-	580	10 (~1.25 V)	S18
NPMC-1000	1.48	55	735	240 (~1.3 V)	S7
CuPt-NC	1.5	250	560	-	S19
MnO_x/C	1.4	190	290	-	S20
$PbMnO_x$	-	40	-	50 (~1.2 V)	S21
$CoMn_2O_4$/NGr	1.48	-	460	-	S22

Table S5. The performance of rechargeable Zn-air batteries with various electrocatalysts.

Catalyst	Recharge ability	Reference
PS-CNS	720 s/cycle for 500 cycles; 100 h	This work
PCN-CFP	600 s/cycle for 50 cycles; 8.3 h	S6
NPMC-1000	600 s/cycle for 600 cycles; 100 h	S7
NCNF-1000	600 s/cycle for 500 cycles; 83 h	S12
Fe@NC	600 s/cycle for 100 cycles; 17 h	S14
c-$CoMn_2$/C	400 s/cycle for 155 cycles; 17 h	S23
NiO/$Ni(OH)_2$	4200 s/cycle for 70 cycles; 83 h	S24
NCNT/CoO-NiO-NiCo	600 s/cycle for 100 cycles; 17 h	S25
LBSCFO-50	600 s/cycle for 100 cycles; 17 h	S26
CoO/N-CNT + NiFe LDH/Ni	200 s/cycle for 60 cycles; 3.3 h	S16
Co_3O_4 NWs	600 s/cycle for 600 cycles; 100 h	S27
Ag-Cu on nickel foam	1200 s/cycle for 100 cycles; 34 h	S28
BNC	600 s/cycle for 66 cycles; 11 h	S29
$LaNiO_3$/N-CNT	600 s/cycle for 75 cycles; 12.5 h	S30

Supplementary video

Video S1. The OER performance of P,S-CNS-CFP (directly used as the working electrode) at an operating potential of 1.56 V.

The video shows (i) the complete setup; (ii) P,S-CNS-CFP before applying a potential; (iii) the generation of O_2 gas on a P,S-CNS-CFP electrode; (iv) that no peeling of the catalysts occurred after testing, showing the strong coupling between P,S-CNS and CFP and the high structural stability of the prepared oxygen catalyst; (v) the generated O_2 gas is efficiently released from the surface of the electrodes in the form of tiny bubbles (rather than accumulating into very large bubbles).

Computational details:

All *Ab initio* calculations were performed with the Vienna *Ab initio* Simulation Package (VASP 5.3.5) using projector augmented wave (PAW) method [S31-S32] with the generalized gradient approximation based on the Perdew–Burke–Ernzerhof (PBE) exchange-correlation functional.[S33] The computational models were built in a hexagonal unit cell repeated along ***a*** and ***b*** directions with a vacuum region of up to 15 Å along ***c*** direction to exclude the mirror interactions. The schematics of our models are shown in figure S17a. For the convenience of identifying the doping and active sites, we name it by alphabetical characters and Arabic numbers in figure S17b and 17c, respectively.

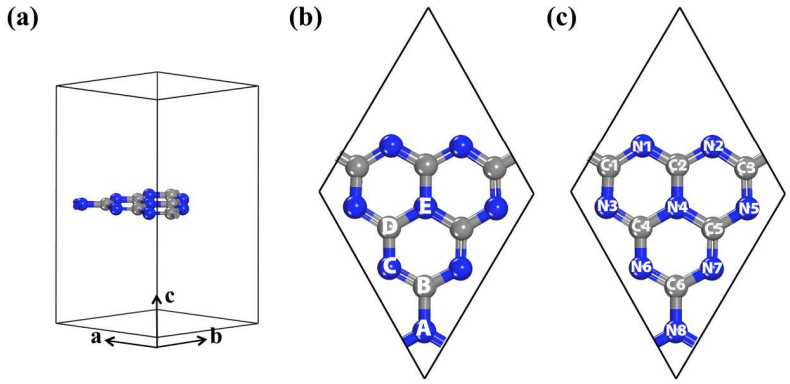

Figure S17. (a) Structure of pure-C_3N_4 unit cell. (b) Alphabetic characters indicating substitutional doping sites and (c) Arabic numbers showing active sites for OER/ORR.

The Brillouin zone was sampled with a K-point grid of 3 × 3 × 1, according to the Monkhorst-Pack scheme.[S34] A plane-wave cutoff energy of 500 eV was employed to control the fineness of this mesh. All investigations for oxygen evolution reaction (OER) and oxygen reduction reaction (ORR) were carried out using fully optimized structures. For structural optimization, Lattice vectors and ionic positions were fully relaxed until the maximum atomic forces were less than 0.04 eV/Å. Then, static calculations of free energy diagrams and overpotential η were performed to estimate OER/ORR activities. Subsequently, we analyzed a volcano-shaped relationship between catalytic activity and the calculated adsorption energies of *O** and *OH**.

We carried out first-principles calculations using density functional theory (DFT) methods to investigate the electrocatalytic activity of OER/ORR of pure- and doped-C_3N_4 systems. The electrocatalytic activities of OER/ORR are estimated by free energy diagrams of the associative mechanism consists of four consecutive proton and electron transfer steps

based on the *HO**, *O** and *HOO** adsorption energies on the surfaces of pure- and doped-C_3N_4. In alkaline media, the four electron reaction steps of OER mechanism were described as followings,

$$OH^- + * \rightarrow OH^* + e^- \quad (1)$$

$$OH^* + OH^- \rightarrow O^* + H_2O(l) + e^- \quad (2)$$

$$O^* + OH^- \rightarrow OOH^* + e^- \quad (3)$$

$$OOH^* + OH^- \rightarrow O^* + O_2(g) + H_2O(l) + e^- \quad (4)$$

where, $*$ represents the active site where *OH* and *O* species can adsorb.

In the ORR reaction, we considered the overall reaction mechanism completely *via* a direct four-electron process in which molecular oxygen is reduced to water without formation of the hydrogen peroxide intermediate, H_2O_2. The ORR mechanism in alkaline environment could occur in the following four electron reaction paths,

$$O_2^* + H_2O(l) + e^- \rightarrow OOH^* + OH^- \quad (5)$$

$$OOH^* + e^- \rightarrow O^* + OH^- \quad (6)$$

$$O_2^* + H_2O(l) + e^- \rightarrow OH^* + OH^- \quad (7)$$

$$OH^* + e^- \rightarrow * + OH^- \quad (8)$$

We calculated the binding energies of the intermediates *O**, *OH**, and *OOH** on the S doped C_3N_4, P doped C_3N_4 and P,S doped C_3N_4 to know the point of the rate limiting step for OER and ORR on various active sites for different structures. The binding energies were calculated as follows,

$$\Delta E_{OH^*} = E(OH^*) - E(*) - (E_{H_2O} - \tfrac{1}{2}E_{H_2}) \quad (9)$$

$$\Delta E_{OOH^*} = E(OOH^*) - E(*) - (2E_{H_2O} - \tfrac{2}{3}E_{H_2}) \quad (10)$$

$$\Delta E_{O^*} = E(O^*) - E(*) - (E_{H_2O} - E_{H_2}) \quad (11)$$

where, $E(*)$, $E(OH^*)$, $E(O^*)$ and $E(OOH^*)$ are the ground state energies of the clean surface and the surfaces adsorbed with *OH**, *O** and *OOH**, respectively. E_{H_2O} and E_{H_2} are the calculated DFT energies of H_2O and H_2 molecules in the gas phase using the approaches

outlined by Norskov et al.[S35] Additionally, we considered the zero-point energy and entropy corrections here. From these calculations, the binding free energies like ΔE_{OH^*}, ΔE_{OOH^*} and ΔE_{O^*} could be written in terms of adsorption free energies, ΔG_{ads}, by the following equation,

$$\Delta G_{ads} = \Delta E_{DFT}^{ads} + \Delta ZPE - T\Delta S \qquad (12)$$

where, T is the temperature and ΔS is the entropy change.

Subsequently, we constructed free energy diagram considering the following four electron reaction paths in equations (13)-(19) at standard conditions.[S35]

For OER reaction:

$$\Delta G_1 = \Delta G_{OH^*} + \mu_{e^-} - \Delta G_{OH^-} - \Delta G_* \qquad (13)$$

$$\Delta G_2 = \Delta G_{O^*} + \Delta G_{H_2O} + \mu_{e^-} - \Delta G_{OH^*} - \Delta G_{OH^-} \qquad (14)$$

$$\Delta G_3 = \Delta G_{OOH^*} + \mu_{e^-} - \Delta G_{O^*} - \Delta G_{OH^-} \qquad (15)$$

$$\Delta G_4 = \Delta G_{O_2} + \Delta G_{H_2O} + \mu_{e^-} - \Delta G_{OOH^*} - \Delta G_{OH^-} - \Delta G_* \qquad (16)$$

For ORR reaction:

$$\Delta G_1 = \Delta G_{OOH^*} + \Delta G_{OH^-} - \Delta G_{O_2^*} - \Delta G_{H_2O} - \mu_{e^-} \qquad (17)$$

$$\Delta G_2 = \Delta G_{O^*} + \Delta G_{OH^-} - \Delta G_{OOH^*} - \mu_{e^-} \qquad (18)$$

$$\Delta G_3 = \Delta G_{OH^*} + \Delta G_{OH^-} - \Delta G_{O^*} - \Delta G_{H_2O} - \mu_{e^-} \qquad (19)$$

$$\Delta G_4 = \Delta G_* + \Delta G_{OH^-} - \Delta G_{OH^*} - \mu_{e^-} \qquad (20)$$

From the free energy diagram, we can deduce an important parameter for electrocatalytic activity that is the magnitude of the potential-determining step ($G^{OER/ORR}$) in four consecutive proton and electron transfer steps. This is the specific reaction step in the four-step mechanism with the largest ΔG, that is, the concluding step to become downhill in free energy as the potential increased [Eq. (21)]:

$$\Delta G^{OER/ORR} = \max\left[\Delta G_1^0, \Delta G_2^0, \Delta G_3^0, \Delta G_4^0\right] \qquad (21)$$

The theoretical overpotential at standard conditions is then given by equation (22):

$$\eta^{OER/ORR} = \left(\frac{G^{OER/ORR}}{e}\right) - 0.401 \qquad (22)$$

In advance, we have premeditated feasible models structures considering heteroatom

doping sites and OER/ORR active sites in C_3N_4 systems to find structures providing the best performance in each of the S-C_3N_4, P-C_3N_4 and P,S-C_3N_4 structures, as shown in figure S17. Our explorations on the OER/ORR activities revealed that the doped-C_3N_4 has the best OER/ORR activities when heteroatoms are substituted into the carbon sites of C_3N_4. And the best OER/ORR activities for the doped-C_3N_4 occur at different active sites, as shown in figure S18.

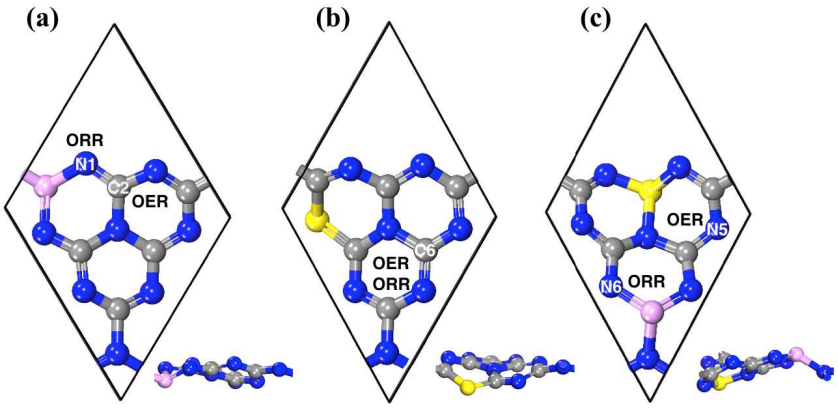

Figure S18. The high performance (a) P-C_3N_4, (b) S-C_3N_4 and (c) P,S-C_3N_4 structures. The best OER/ORR active sites are inset with element numbers.

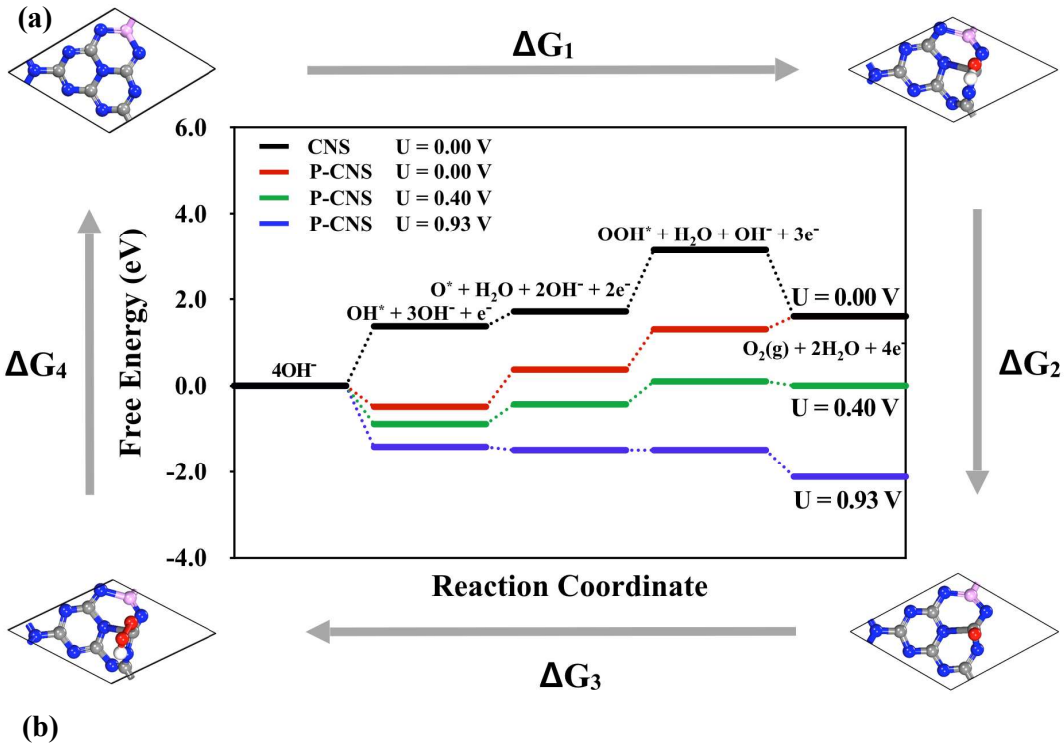

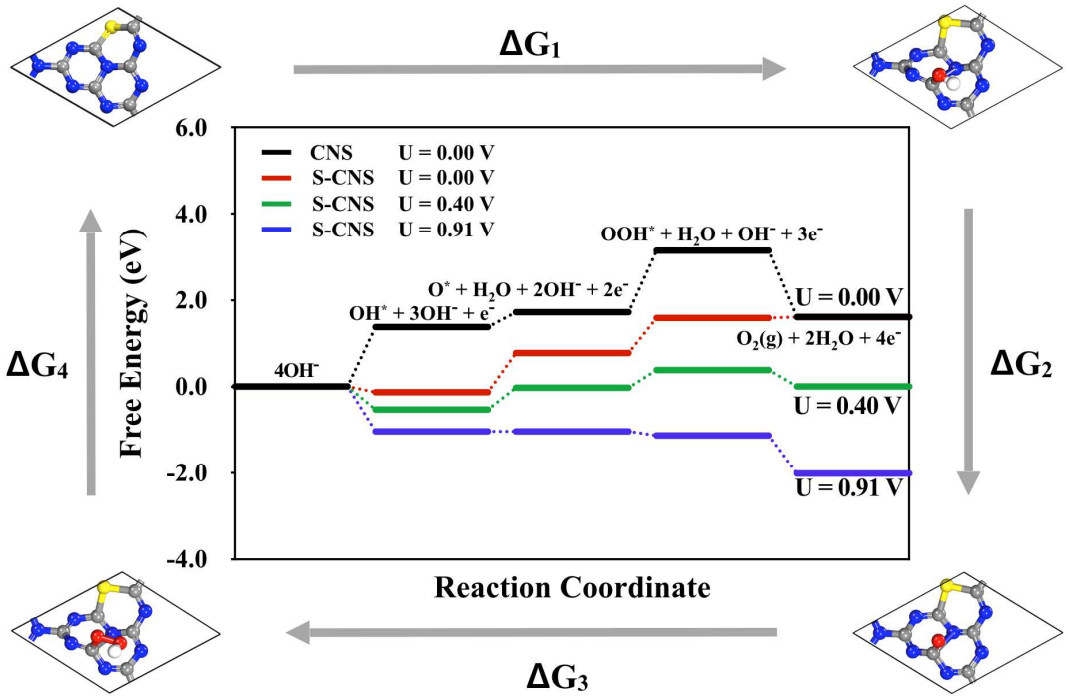

Figure S19. Free energy diagrams of (a) P-CNS, and (b) S-CNS for the OER pathway at several potentials.

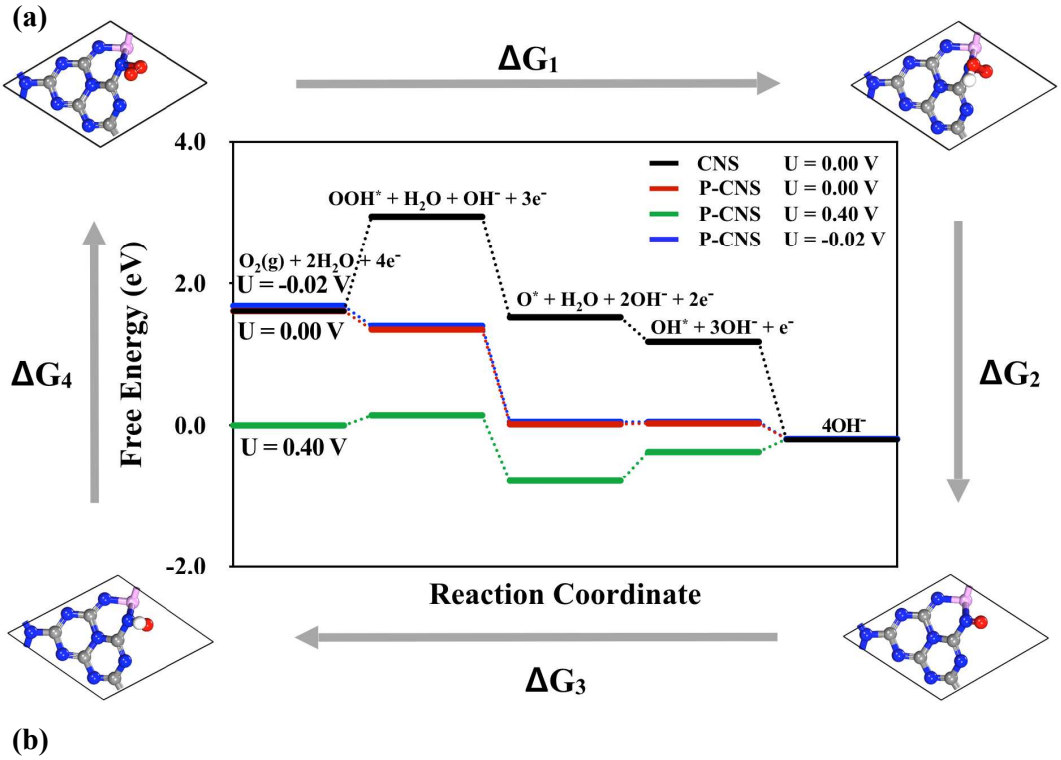

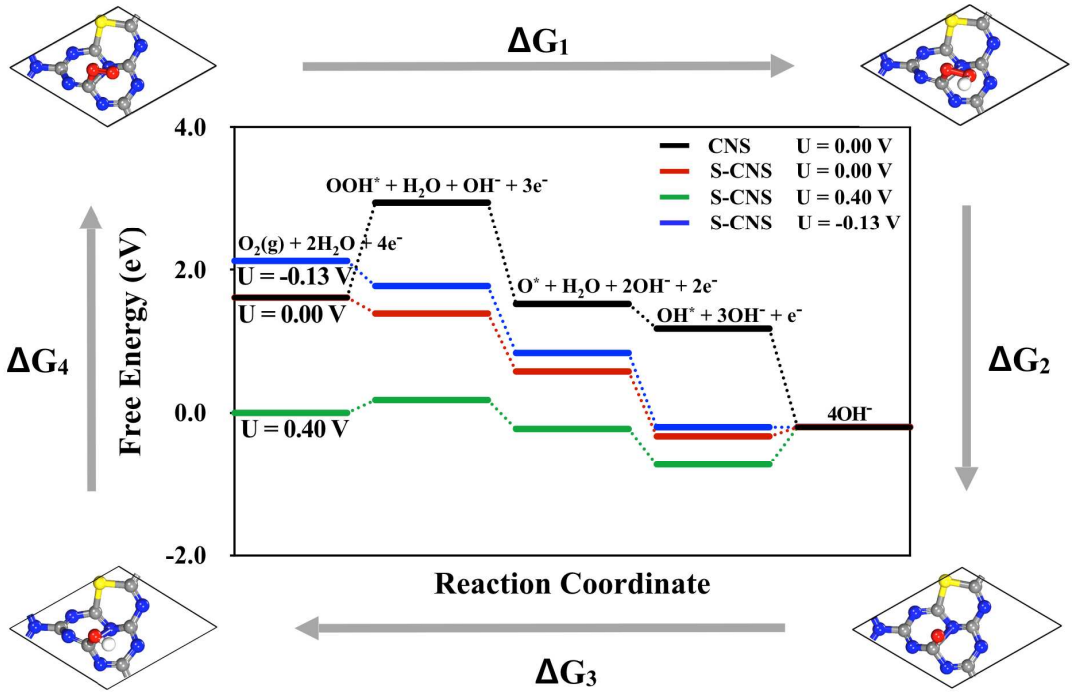

Figure S20. Free energy diagrams of (a) P-CNS, and (b) S-CNS for the ORR pathway at several potentials.

REFERENCES

S1. Cheng, Y.; Huang, L.; Xiao, X.; Yao, B.; Yuan, L.; Li, T.; Hu, Z.; Wang, B.; Wan, J.; Zhoun, J. Flexible and Cross-Linked N-Doped Carbon Nanofiber Network for High Performance Freestanding Supercapacitor Electrode. *Nano Energy* **2015,** *15*, 66–74.

S2. Zhang, G.; Zhang, M.; Ye, X.; Qiu, X.; Lin, S.; Wang, X. Iodine Modified Carbon Nitride Semiconductors as Visible Light Photocatalysts for Hydrogen Evolution. *Adv. Mater.* **2014,** *26*, 805–809.

S3. Xiang, Q.; Yu J.; Jaroniec, M. Preparation and Enhanced Visible-Light Photocatalytic H_2-Production Activity of Graphene/C_3N_4 Composites. *J. Phys. Chem. C*, **2011,** *115*, 7355-7363.

S4. Wang, Y.; Bai, X.; Pan, C.; He J.; Zhu, Y. Enhancement of Photocatalytic Activity of Bi_2WO_6 Hybridized With Graphite-Like C_3N_4. *J. Mater. Chem.,* **2012,** *22,* 11568-11573.

S5. Zhang, Y.; Mori, T.; Ye, J.; Antonietti, M. Phosphorus-Doped Carbon Nitride Solid: Enhanced Electrical Conductivity and Photocurrent Generation. *J. Am. Chem. Soc.* **2010,** *132*, 6294–6295.

S6. Ma, T.; Ran, J.; Dai, S.; Jaroniec, M.; Qiao, S. Phosphorus-Doped Graphitic Carbon Nitrides Grown *in Situ* on Carbon-Fiber Paper: Flexible and Reversible Oxygen Electrodes. *Angew. Chem. Int. Ed.* **2015,** *54*, 4646–4650.

S7. Zhang, J.; Zhao, Z.; Xia, Z.; Dai, L. A Metal-Free Bifunctional Electrocatalyst for Oxygen Reduction and Oxygen Evolution Reactions. *Nat. Nanotechnol.* **2015,** *10*, 444-452.

S8. Tian, G.; Zhao, M.; Yu, D.; Kong, X.; Huang, J.; Zhang, Q.; Wei, F. Nitrogen-Doped Graphene/Carbon Nanotube Hybrids: *In Situ* Formation on Bifunctional Catalysts and Their Superior Electrocatalytic Activity for Oxygen Evolution/Reduction Reaction. *Small* **2014,** *10*, 2251−2259.

S9. Masa, J.; Xia, W.; Sinev, I.; Zhao, A.; Sun, Z.; Grützke, S.; Weide, P.; Muhler, M.; Schuhmann, W. Mn_xO_y/NC and Co_xO_y/NC Nanoparticles Embedded in a Nitrogen-Doped Carbon Matrix for High-Performance Bifunctional Oxygen Electrodes. *Angew. Chem. Int. Ed.* **2014,** *53*, 8508–8512.

S10. Wang, D.; Chen, X.; Evans, D.; Yang, W. Well-Dispersed Co_3O_4/Co_2MnO_4 Nanocomposites as a Synergistic Bifunctional Catalyst for Oxygen Reduction and Oxygen Evolution Reactions. *Nanoscale* **2013,** *5,* 5312-5315.

S11. Mao, S.; Wen, Z.; Huang, T.; Hou, Y.; Chen, J. High-Performance Bi-Functional Electrocatalysts of 3D Crumpled Graphene–cobalt Oxide Nanohybrids for Oxygen Reduction and Evolution Reactions. *Energy Environ. Sci.* **2014,** *7*, 609–616.

S12. Liu, Q.; Wang, Y.; Dai, L.; Yao, J. Scalable Fabrication of Nanoporous Carbon Fiber Films as Bifunctional Catalytic Electrodes for Flexible Zn-Air Batteries. *Adv. Mater.* **2016,** *28*, 3000–3006.

S13. Jahan, M.; Liu, Z.; Loh, K. A Graphene Oxide and Copper-Centered Metal Organic Framework Composite as a Tri-Functional Catalyst for HER, OER, and ORR. *Adv. Funct. Mater.* **2013,** *23*, 5363–5372.

S14. Wang, J.; Wu, H.; Gao, D.; Miao, S.; Wang, G.; Bao, X. High-Density Iron Nanoparticles Encapsulated Within Nitrogen-Doped Carbon Nanoshell as Efficient Oxygen Electrocatalyst for Zinc–air Battery. *Nano Energy* **2015,** *13*, 387-396.

S15. Cao, R.; Thapa, R.; Kim, H.; Xu, X.; Kim, M.; Li, Q.; Park, N.; Liu, M.; Cho, J. Promotion of Oxygen Reduction by a Bio-Inspired Tethered Iron Phthalocyanine Carbon Nanotube-Based Catalyst. *Nat. Commun.* **2013,** *4*, 2076.

S16. Li, Y.; Gong, M.; Liang, Y.; Feng, J.; Kim, J.; Wang, H.; Hong, G.; Zhang, B.; Dai, H. Advanced Zinc-Air Batteries Based on High-Performance Hybrid Electrocatalysts. *Nat. Commun.* **2013,** *4*, 1805.

S17. Liu, Y.; Chen, S.; Quan, X.; Yu, H.; Zhao, H.; Zhang, Y.; Chen, G. Boron and Nitrogen Codoped Nanodiamond as an Efficient Metal-Free Catalyst for Oxygen Reduction Reaction. *J. Phys. Chem. C,* **2013,** *117*, 14992–14998.

S18. Prabu, M.; Ketpang, K.; Shanmugam, S. Hierarchical Nanostructured $NiCo_2O_4$ as an Efficient Bifunctional Non-Precious Metal Catalyst for Rechargeable Zinc–air Batteries. *Nanoscale,* **2014,** *6,* 3173-3181.

S19. Dhavale, V.; Kurungot, S. Cu–Pt Nanocage With 3-D Electrocatalytic Surface as an Efficient Oxygen Reduction Electrocatalyst for a Primary Zn–Air Battery. *ACS Catal*. **2015,** *5*, 1445-1452.

S20. Lee, J.; Park, G.; Lee, H.; Kim, S.; Cao, R.; Liu, M.; Cho, J. Ketjenblack Carbon Supported Amorphous Manganese Oxides Nanowires as Highly Efficient Electrocatalyst for Oxygen Reduction Reaction in Alkaline Solutions. *Nano Lett.* **2011,** *11*, 5362-5366.

S21. Yang, T.; Venkatesan, S.; Lien, C.; Chang, J.; Zen, J. Nafion/lead Oxide–manganese Oxide Combined Catalyst for Use as a Highly Efficient Alkaline Air Electrode in Zinc–air Battery. *Electrochim. Acta,* **2011,** *56*, 6205-6210.

S22. Qiu, Y.; Xin, L.; Li, W. Electrocatalytic Oxygen Evolution over Supported Small Amorphous Ni–Fe Nanoparticles in Alkaline Electrolyte. *Langmuir* **2014,** *30,* 7893-7901.

S23. Li, C.; Han, X.; Cheng, F.; Hu, Y.; Chen, C.; Chen, J. Phase and Composition Controllable Synthesis of Cobalt Manganese Spinel Nanoparticles Towards Efficient Oxygen Electrocatalysis. *Nat. Commun*. **2015,** *6,* 7345.

S24. Lee, D.; Fu, J.; Park, M.; Liu, H.; Kashkooli, A.; Chen, Z. Self-Assembled NiO/Ni(OH)$_2$ Nanoflakes as Active Material for High-Power and High-Energy Hybrid Rechargeable Battery. *Nano Lett*. **2016,** *16,* 1794−1802.

S25. Liu, X.; Park, M.; Kim, M.; Gupta, S.; Wu, G.; Cho, J. Integrating NiCo Alloys With Their Oxides as Efficient Bifunctional Cathode Catalysts for Rechargeable Zinc–Air Batteries. *Angew. Chem. Int. Ed.* **2015,** *54,* 9654 –9658.

S26. Jung, J.; Risch, M.; Park, S.; Kim, M.; Nam, G.; Jeong, H.; Horn, Y.; Cho, J. Optimizing Nanoparticle Perovskite for Bifunctional Oxygen Electrocatalysis. *Energy Environ. Sci.*, **2016,** *9*, 176-183.

S27. Lee, D.; Choi, J.; Feng, K.; Park, H.; Chen, Z. Advanced Extremely Durable 3D Bifunctional Air Electrodes for Rechargeable Zinc–air Batteries. *Adv. Energy Mater.* **2014,** *4*, 1301089.

S28. Jin, Y.; Chen, F. Facile Preparation of Ag-Cu Bifunctional Electrocatalysts for Zinc-Air Batteries. *Electrochim. Acta* **2015,** *158*, 437-445.

S29. Zhuang, X.; Gehrig, D.; Forler, N.; Liang, H.; Wagner, M.; Hansen, M.; Laquai, F.; Zhang, F.; Feng, X. Conjugated Microporous Polymers With Dimensionality-Controlled Heterostructures for Green Energy Devices. *Adv. Mater.* **2015,** *27*, 3789-3796.

S30. Chen, Z.; Yu, A.; Higgins, D.; Li, H.; Wang, H.; Chen, Z. Highly Active and Durable Core–Corona Structured Bifunctional Catalyst for Rechargeable Metal–Air Battery Application. *Nano Lett.* **2012,** *12*, 1946–1952.

S31. Blochl, P. Projector Augmented-Wave Method. *Phys. Rev. B.* **1994,** *50*, 17953.

S32. Kresse, G.; Joubert, D. From Ultrasoft Pseudopotentials to the Projector Augmented-Wave Method. *Phys. Rev. B.* **1999,** *59,* 1758.

S33. Perdew, J.; Burke, K.; Ernzerhof, M. Generalized Gradient Approximation Made Simple. *Phys. Rev. Lett.* **1996,** *77,* 3865.

S34. Monkhorst, H.; Pack, J. Special Points for Brillouin-Zone Integrations. *Phys. Rev. B,* **1976,** *13,* 5188.

S35. Man, I.; Su, H.; Calle-Vallejo, F.; Hansen, H.; Martinez, J.; Inoglu, N.; Kitchin, J.; Jaramillo, T.; Norskov, J.; Rossmeisl, J. Universality in Oxygen Evolution Electrocatalysis on Oxide Surfaces. *ChemCatChem,* **2011,** *3*, 1159-1165.